

1 **Linking glacially modified waters to catchment-scale subglacial discharge using**
2 **autonomous underwater vehicle observations**

3
4 Laura A. Stevens¹, Fiamma Straneo², Sarah B. Das³, Albert J. Plueddemann², Amy L. Kukulya⁴,
5 and Mathieu Morlighem⁵

6 ¹Massachusetts Institute of Technology/Woods Hole Oceanographic Institution Joint Program in
7 Oceanography/Applied Ocean Science and Engineering, Woods Hole, MA 02543, USA

8 ²Department of Physical Oceanography, Woods Hole Oceanographic Institution, Woods Hole,
9 MA 02543, USA

10 ³Department of Geology and Geophysics, Woods Hole Oceanographic Institution, Woods Hole,
11 MA 02543, USA

12 ⁴Department of Applied Ocean Physics and Engineering, Woods Hole Oceanographic Institution,
13 Woods Hole, MA 02543, USA

14 ⁵Department of Earth System Science, University of California, Irvine, Croul Hall, Irvine, CA
15 92697, USA

16 Correspondence to: L. A. Stevens (stevensl@mit.edu)

17 **Abstract**

18 Measurements of near-ice (<200 meters) hydrography and near-terminus subglacial hydrology
19 are lacking due in large part to the difficulty in working at the margin of calving glaciers. Here
20 we pair detailed hydrographic and bathymetric measurements collected with an Autonomous
21 Underwater Vehicle as close as 150 meters from the ice/ocean interface of the Saqqarliup
22 sermia/Sarqardleq Fjord system, West Greenland, with modeled and observed subglacial
23 discharge locations and magnitudes. We find evidence of two main types of subsurface glacially
24 modified water (GMW) with distinct properties and locations. The two GMW locations also
25 align with modeled runoff discharged at separate locations along the grounded margin
26 corresponding with two prominent subcatchments beneath Saqqarliup sermia. Thus, near-ice
27 observations and subglacial discharge routing indicate that runoff from this glacier occurs
28 primarily at two discrete locations and gives rise to two distinct glacially modified waters.
29 Furthermore, we show that the location with the largest subglacial discharge is associated with
30 the lighter, fresher glacially modified watermass. This is qualitatively consistent with results
31 from an idealized plume model.

32

33 **1. Introduction**

34 Greenland Ice Sheet mass loss quadrupled over the last two decades, contributing roughly
35 7.4 mm to global sea level rise from 1992-2011 (Shepherd et al., 2012), and increasing
36 freshwater inputs into the North Atlantic (Bamber et al., 2012). Ice sheet mass loss occurs
37 through runoff of surface melt, ice discharge through iceberg calving, and submarine melt at
38 marine-terminating outlet glacier margins (van den Broeke et al., 2009; Enderlin et al., 2014).
39 The synchronous retreat and speedup of marine-terminating glaciers in southeast Greenland in

40 the early 2000s was likely initiated by a dynamic change at marine termini (van den Broeke et
41 al., 2009; Rignot and Kanagaratnam, 2006; Thomas et al., 2009), and points towards common
42 external forcings from the warming atmosphere (Box et al., 2009) and/or ocean around
43 Greenland (Straneo and Heimbach, 2013), though the exact forcing mechanisms and relative
44 magnitudes remain unclear (Joughin et al., 2012; Straneo et al., 2013).

45 Increased submarine melt rates at outlet glacier marine termini may be a leading cause of
46 Greenland Ice Sheet outlet glacier speed up and retreat (Holland et al., 2008; Joughin et al.,
47 2012; Motyka et al., 2013; Post et al., 2011). The heat to drive submarine melting is supplied by
48 waters from the subpolar North Atlantic and Arctic seas, whose circulation inside the fjords is a
49 result of processes across a range of spatiotemporal scales (Jackson et al., 2014; Straneo et al.,
50 2010). Ultimately, melt rates are affected by ocean properties (temperature and stratification) and
51 circulation in near-ice waters (<200 m) (Jenkins et al., 2010). Submarine melting is thought to be
52 enhanced in summer as a result of meltwater runoff along the ice sheet bed entering the fjord
53 across the grounding line as subglacial discharge, which provides an additional buoyancy source
54 alongside submarine melt for initiating buoyant plumes along the terminus face (Jenkins, 1999,
55 2011; Sciascia et al., 2013; Xu et al., 2013). Relatively fresh waters rising in the core of these
56 plumes become denser as they entrain salty ambient fjord waters, and this entrainment driven by
57 plumes serves as a mechanism for transporting ambient fjord waters to the glacier face (Jenkins,
58 1999, 2011; Sciascia et al., 2013; Xu et al., 2013).

59 Plume theory and models combined with melt rate parameterizations suggest that higher
60 subglacial discharge rates are associated with faster flows and entrainment of a greater volume of
61 ambient fjord waters leading to higher submarine melt rates (Jenkins, 1999, 2011; Sciascia et al.,
62 2013; Xu et al., 2013; Carroll et al., 2015), however ocean property and plume measurements

63 needed to inform and validate model simulations and theory are lacking due to difficulty in
64 working at the margin of calving glaciers (Straneo and Cenedese, 2015). As a result, current
65 modeling-sourced estimates of submarine melt rates at tidewater glaciers and their sensitivity to
66 external forcings of the near-ice environment are highly uncertain, and based on unconstrained
67 models of plume dynamics using ice/ocean boundary parameterizations forced by far field (>1
68 km) ocean property measurements and largely unknown subglacial discharge magnitude and
69 distribution (Jenkins, 2011; Kimura et al., 2014; Sciascia et al., 2013; Slater et al., 2015; Xu et
70 al., 2012, 2013). For example, in a recent numerical study the spatial distribution of subglacial
71 discharge along the grounding line was found to have a large effect on both the total submarine
72 melt rate and its distribution along marine termini (Slater et al., 2015). With a lack of
73 observations of both the near-ice environment and subglacial discharge configurations, we are
74 unable to define likely subglacial discharge scenarios and their associated influence on ice/ocean
75 interactions, resulting in an inadequate and untested understanding of how tidewater glaciers
76 respond to oceanic forcing now and in the future (Straneo and Cenedese, 2015). Specifically,
77 ocean measurements collected at distances >1 km from the glacier terminus provide limited
78 information on the near-ice processes because the signals of glacial modification have, by that
79 time, largely been smeared by lateral mixing processes. Indeed, the picture that emerges from
80 such far-field measurements is of a horizontally invariant overturning cell(s) (Chauché et al.,
81 2014; Inall et al., 2014; Johnson et al., 2011; Mortensen et al., 2011; Straneo et al., 2011;
82 Sutherland et al., 2014).

83 In this study, we present fjord hydrography and bathymetry measurements from the near-
84 ice environment of a tidewater glacier in west Greenland (Fig. 1) that allow us to reconstruct the
85 distribution of subglacial discharge and provide key details on the ice-ocean exchanges. We do

86 this by identifying the distribution of Glacially Modified Waters (GMW)—a product of ambient
87 fjord waters mixing with subglacial discharge and glacial melt, including cooling due the melting
88 of ice (Jenkins, 2011; Straneo et al., 2011)—within a few 100 m of the glacier face, and by
89 delineating the subglacial catchments that route subglacial meltwater to discharge locations
90 along the grounded terminus. These hydrographic measurements were obtained primarily in July
91 2012, using a REMUS-100 (Remote Environmental Measuring UnitS) Autonomous Underwater
92 Vehicle (AUV) (Fig. 2 a) to observe the temperature, salinity, and turbidity of waters in
93 Sarqardleq Fjord (SF) from ~2 km away to within a couple hundred meters of Saqqarliup sermia
94 (SS) (Sarqardliup sermia in Old Greenlandic), a medium-sized tidewater glacier in West
95 Greenland (68.90° N 50.32° W) (Fig. 1). This novel, high-risk field campaign was successful in
96 obtaining multiple vertical sections of fjord water properties as close as 150 ± 25 m from the
97 terminus as well as detailed bathymetry of the previously unmapped fjord.

98

99 **2. Field Campaign**

100

101 **2.1. REMUS-100 AUV**

102 The REMUS-100 AUV is a small (1.8-m long) and light (45 kilograms) vehicle, rated to
103 100-m-depth that has been modified for under-ice exploration (Plueddemann et al., 2012) (Fig. 2
104 a). REMUS environmental sensors included a Neil Brown Ocean Systems conductivity-depth-
105 temperature (CTD) sensor, a WetLabs Environmental Characterization Optics (ECO) Triplet
106 sensor, and a Teledyne/RDI dual (upward and downward looking) 1200 kHz Acoustic Doppler
107 Current Profiler (ADCP). The ECO Triplet provides measurements of turbidity from backscatter
108 at 660 nm. At the surface, REMUS communications include Iridium satellite telemetry,

109 FreeWave 900 MHz radio acoustic data telemetry, WiFi for local area network for wireless
110 testing and configuration, and a Global Positioning System (GPS) receiver for location fixes at
111 the start and end of missions. At depth, REMUS navigates by acoustically ranging to a network
112 of three moored Low Frequency (LF 10 kHz) Long BaseLine (LBL) transponders (Fig. 3). The
113 vehicle continuously updates its position while underway through a combination of dead
114 reckoning algorithms (which incorporate compass data, as well as propeller turns, water velocity
115 and bottom track data from the ADCP), LBL fixes, and surface GPS fixes when available (see
116 Plueddemann et al. 2012).

117 Field operations from the shore and in small boats took place from 17–27 July 2012
118 (DOY 199–209). SF is largely free of icebergs after spring sea ice break up, though frequent
119 calving along the SS terminus prevents boat travel within ~200 m of the terminus. REMUS
120 experienced navigational challenges in fjord environment due to a confluence of factors
121 including a strong surface pycnocline, loud and variable noise from calving and overturning of
122 icebergs, and heavy ice conditions preventing some GPS fixes. Transects presented here include
123 occasional deviations on the order of 5 to 50 m perpendicular to mission tracks. Data collected
124 during mission track deviations are accepted and collapsed back onto the transect line.

125 Deployed over the side of a small fishing boat, and eventually from the shore, 11
126 REMUS missions were completed over 9 days for both engineering and science objectives.
127 Although a minor issue for the localization of water properties, the navigation challenges and
128 track-line deviations caused significant uncertainties in the conversion from vehicle-relative to
129 earth-referenced velocities. As a result, only measurements from the CTD and ECO Triplet are
130 presented here. Combinations of yo-yo, fixed-depth, and fixed-altitude above bottom sampling
131 paths along transects parallel to the glacier face were used to acquire vertical sections of SF

132 water properties. In total, 5 transects of temperature, salinity, and turbidity along 5 terminus-
133 parallel sections (R1–R5 (Fig. 3)) at distances 150 to 1500 ± 25 m from the terminus selected
134 based on REMUS navigation quality and best across- and along-fjord coverage are presented in
135 this paper (Table 1).

136

137 **2.2. Hydrographic and turbidity data**

138 Profiles and sections presented here are made from along-track edited and smoothed
139 REMUS CTD and ECO data. REMUS temperature and salinity data were edited with the
140 removal of occasional erroneous points identified by an along-track first difference filter of
141 density calculated from the temperature and salinity measurements. First differences of >0.1
142 sigma were removed, affecting 0.2% of the data. Turbidity values were capped at 10
143 Nephelometric Turbidity Units (NTU). Raw temperature and salinity data were obtained at 0.22
144 s intervals, while turbidity measurements were taken at 1.15 s intervals. Temperature, salinity,
145 and turbidity measurements were interpolated to 0.5 s and then averaged over 2 s to obtain
146 smoothed, along-track data for all sensors on a common timebase with along-track resolution of
147 3.2–3.6 m (based on typical vehicle speeds that ranged between 1.6–1.8 m s^{-1}). Contour maps of
148 observed variables versus depth and distance were created from the REMUS mission tracks by
149 optimal interpolation (kriging) of measurements collapsed along glacier face-parallel transect
150 lines (Fig. 4). Simple, linear fits to computed autocorrelation were used for temperature, salinity,
151 and turbidity. Kriging was completed over a depth and along-track distance range slightly larger
152 than the data range, with a vertical resolution of 2 m and a horizontal resolution of 100 m, based
153 on the along-track resolution of 3 m and the horizontal distance between REMUS mid-depth

154 sample lines of 100 m, respectively. Sensitivity tests of different kriging models and linear slopes
155 yielded little impact on resulting sections, demonstrating a robust kriging methodology.

156 Several shipboard CTD casts, collected using an RBR XR 620 CTD during the field
157 campaign, are presented to supplement the REMUS observations (Fig. 6). Eight shipboard CTD
158 casts were taken along the R1 transect (Fig. 3), 8 casts were taken along cross-fjord sections in
159 the outer SF (>10 km from the SS terminus) (triangles in Fig. 7 a), and 3 casts were taken
160 roughly at the R5 midpoint, northeastern end, and southwestern end (Fig. 3). REMUS and CTD
161 measurements were cross-calibrated by comparing REMUS R1 measurements with the 8 CTD
162 casts taken along the R1 transect immediately following the completion of the REMUS R1
163 mission. θ , S, and depth offsets were found to be 0.0015 °C, -0.05 PSU, and -2.5 m respectively,
164 between the CTD and REMUS measurements. The RBR XR 620 CTD was calibrated before and
165 after the fieldwork, but the REMUS CTD was not. REMUS measurements were therefore
166 adjusted by 2.5 m to match the CTD observations, and this offset is assumed to have remained
167 constant throughout the campaign.

168

169 **2.3. Bathymetric Data**

170 Detailed bathymetry of the previously unmapped SF was obtained through depth
171 measurements from a shipboard single-beam depth sounder, a shipboard ADCP, and the REMUS
172 downward looking ADCP in bottom-track mode (Fig. 3). After removing occasional spikes in
173 the REMUS ADCP depth soundings (outliers on order 15 m deeper than background), depth
174 measurements across the sampling platforms at crossover points were consistent within <4 m.
175 Coastline positions were assigned a depth of 0 m, and were obtained from digitizing a June 19,
176 2012 Landsat image (30-m horizontal resolution). Depth measurements were combined across

177 platforms by calculating a binned average depth measurement over a 25 x 25-m grid across the
178 fjord. The Barnes Objective Analysis (Barnes, 1994) was used to interpolate the binned depth
179 measurements with a 175 x 175-m search radius to create the bathymetry shown in Figure 3. The
180 bathymetry product aligns well with the binned depth measurements (less than 1 m offsets)
181 except in the location of the northern side of the seamount (68.92° N 50.34° W), which contains
182 the maximum offset from the gridded depth measurements at ± 5 m. Due to low data coverage,
183 the Barnes Objective Analysis was not extended to the outer regions of SF. However, with depth
184 measurements from the shipboard echosounder we have mapped the fjord centerline depth to the
185 confluence of SF and Tasiussaq Fjord, 15-km from the SS terminus (Figs. 1, 7 a).

186

187 **3. Physical Setting: The Sarqardleq Fjord/Saqqarliup sermia outlet glacier system**

188

189 **3.1. Fjord bathymetry, subglacial topography, and historical terminus positions**

190 The Saqqarliup sermia/Sarqardleq Fjord (SS/SF) outlet glacier/fjord system is located in
191 West Greenland roughly 30 km south of Jakobshavn Isbræ (Fig. 1). SS is a marine terminating
192 outlet glacier with a 6-km wide terminus and an upstream subglacial catchment area of 400 ± 50
193 km^2 (Fig. 7a, Table 3; methods described in section 3.2). We estimate total annual runoff out of
194 this catchment to be on the order of $1 \text{ km}^3 \text{ yr}^{-1}$ using Regional Atmospheric Climate Model
195 version 2.3 (RACMO2.3) runoff values (van den Broeke et al., 2009) (methods described in
196 section 3.2). A bedrock trough 100–150 m below sea level extends 15 km inland from the
197 terminus, and continues further inland as a bedrock trough above sea level (Morlighem et al.,
198 2014) (Fig. 7 a). The SS centerline ice thickness is ~ 200 m at the terminus and increases inland
199 (Morlighem et al., 2014) (Fig. 7 a). The Saqqarliup sermia terminus position has been relatively

200 stable in comparison to the large terminus retreats observed at other Greenland tidewater glaciers
201 (Moon and Joughin, 2008) based on our analyses of LANDSAT imagery from 1979 to present
202 (Fig. 2 b). Modest advance and retreat phases on the order of ± 500 m are observed over recent
203 decades, with a net retreat of ~ 1 km within the center third of the glacier terminus observed from
204 1992 to present (Fig. 2 b). Average flow velocities within the SS outlet glacier during the 2007–
205 2009 winters were on order $125\text{--}175$ m yr⁻¹, with the center third of the SS terminus reaching
206 speeds of 200 m yr⁻¹ (Joughin et al., 2013).

207 The Sarqardleq-Tasiussaq fjord system is the southern side fjord off the larger, deeper
208 Jakobshavn Isbræ (JI) fjord, which connects the largest and fastest Greenland ice stream (JI) to
209 Disko Bugt (Fig. 1a). From the SS terminus, the shallower Sarqardleq-Tasiussaq Fjord system
210 extends roughly 30 km to the northwest before reaching JI fjord. SF meets Tasiussaq Fjord over
211 a previously unknown 70-m-deep sill, 15 km from the SS terminus (Figs. 1 & 7 a). Tasiussaq
212 Fjord meets JI fjord over an at most 125-m-deep sill (Gladish et al., 2015a) 30 km from the SS
213 terminus (Fig. 1). Waters along the SS terminus range from 20–150-m-depth, and are deepest in
214 two troughs near the center of the glacier (Fig. 2, Table 3). Both SS lateral terminus regions are
215 grounded in relatively shallow lagoons (<20 m) (Fig. 3). A 40-m-deep seamount is located 2.5
216 km from the vertical SS calving face (Fig. 3).

217

218 **3.2. Subglacial catchment and runoff**

219 To first order, subglacial catchments are defined by ice sheet surface and bed topography,
220 which governs subglacial hydraulic potential at the bed (Cuffey and Patterson, 2010). Gradients
221 in subglacial hydraulic potential at the ice-sheet bed do not completely dictate subglacial
222 meltwater pathways due to the constantly evolving subglacial hydraulic system over the summer

223 melt season (Andrews et al., 2014; Chandler et al., 2013; Hewitt et al., 2012; Schoof, 2010), but
224 subglacial hydraulic potential gradients are likely the dominant regional factor. This is supported
225 by recent modeling studies, which find a strong topographic control of channelized subglacial
226 meltwater routing over Greenland Ice Sheet outlet glaciers (Banwell et al., 2013; Palmer et al.,
227 2011).

228 The SS catchment area was determined based on streamline analysis through subglacial
229 hydraulic potential gradient fields to estimate which path water parcels located at the bed under
230 inland ice will follow out to the coast. The downslope subglacial hydraulic potential gradient, $-\nabla\Phi_h$,
231 was calculated following:

$$232 \quad -\nabla\Phi_h = -\rho_i g [f_w \nabla S + [\rho_w/\rho_i - f_w] \nabla B] \quad \text{eq. 1}$$

233 where ρ_i is the density of ice, ρ_w is the density of freshwater, g is the gravitational acceleration,
234 f_w is the flotation fraction, and ∇S and ∇B are the surface and bed gradients, respectively (Cuffey
235 and Patterson, 2010; Shreve, 1972). We assume water at the bed flows along the steepest
236 subglacial hydraulic potential gradient (Shreve, 1972). We used two widely available bedrock
237 elevation maps, Bamber et al. (2013) and Morlighem et al. (2014) (hereafter BBM2013 and
238 MBM2014) to calculate $-\nabla\Phi_h$ across a 1-km by 1-km grid (Bamber et al. 2013) and 150-m by
239 150-m grid (Morlighem et al. 2014) equivalent to the resolution of each bedrock elevation map.
240 MBM2014 beneath SS was updated from the previously published map by adding our SF
241 bathymetry measurements as a boundary constraint along the SS terminus in this otherwise data-
242 sparse region. The MBM2014 used in this study is available online as IceBridge BedMachine
243 Greenland, Version 2 from the National Snow and Ice Data Center
244 (<http://nsidc.org/data/docs/daac/icebridge/idbmg4/index.html>). Surface ice gradients (∇S) are
245 calculated from the Greenland Ice Mapping Project (GIMP) Digital Elevation Model (Howat et

246 al., 2014). The flotation fraction was set to $f_w = 1$ (basal water pressures are equal to ice
247 overburden pressure), which resulted in the maximum catchment area possible based on basal
248 hydraulic gradients in this region.

249 Surface runoff in the SS catchment for 2012 was determined from bilinear interpolation
250 of the 11-km grid resolution RACMO2.3 runoff values (3 grid cells within SS catchment) (van
251 den Broeke et al., 2009) to the 1-km grid from BMB2013 and the 150-m grid from MBM2014
252 (Fig. 7 a). Portions of the catchment lower than 400 m.a.s.l. were prescribed the same runoff
253 values as the RACMO2.3 grid point within the catchment at 432 m a.s.l. (68.82° N 50.19° W)
254 (Fig. 7 a), as there are no RACMO2.3 grid points at lower elevations within the catchment. We
255 assume that the ice-sheet bed is impermeable (does not store water) over the timescales
256 considered here, and that all surface runoff is transferred immediately to the bed directly beneath
257 the location of runoff formation at the ice sheet surface.

258

259 **4. Results**

260

261 **4.1 Glacially Modified Water (GMW) temperature, salinity, and turbidity properties in** 262 **Sarqardleq Fjord**

263 The summer Sarqardleq fjord waters are characterized by a ~10–20-m fresh and
264 relatively warm surface layer overlying a thick layer of weakly stratified, relatively salty
265 ($S=30.5\text{--}32.5$) and cold ($\theta \approx 1\text{ }^\circ\text{C}$) waters (Table 2, Fig. 5 a, b). The summer fjord waters are the
266 same as the Surface Waters (SW) and Ilulissat Icefjord Waters (IIW) observed by recent
267 hydrographic surveys throughout Ilulissat Icefjord (Gladish et al., 2015a, 2015b). SW are a
268 mixture of IIW and fresher, warmer waters originating from local freshwater sources and

269 warmed by summer atmospheric forcing. IIW originates from Arctic Waters observed in Disko
270 and Baffin Bays (Gladish et al., 2015b) that enter SF after crossing sills at the mouth of JI fjord
271 (Schumann et al., 2012), the confluence of JI fjord and Tasiussaq fjord (Gladish et al., 2015a),
272 and the mouth of SF (Fig. 1). These summer fjord waters are observed in the outer SF by a set of
273 far-field CTD profiles taken near the fjord mouth more than 10 km from the SS terminus
274 (triangles in Fig. 7 a). We define ambient fjord waters as the average of these far-field CTD
275 profiles (red profile in Figs. 5 & 6).

276 Near the glacier we observe a range of water masses not found in the outer fjord. These
277 waters are generally colder, fresher, and more turbid than waters near the mouth of the fjord (Fig.
278 5 a, b). The REMUS sections reveal two distinct Glacially Modified Waters (GMW), which we
279 refer to as GMW1 and GMW2 (Fig. 4, Table 2). GMW1 and GMW2 are cold anomalies with a
280 high turbidity signal that are most evident at two distinct locations (Fig. 4). GMW1 is observed
281 in the southwestern ends of R1–R5 at ~40-m depth, while GMW2 is observed in the northeastern
282 ends of R1–R5 at ~60 m depth (Fig. 4). Both GMW1's and GMW2's temperature and turbidity
283 anomalies are most pronounced close to the glacier (Fig. 4 a–c), and decrease as these waters
284 spread away from the glacier (Fig. 4 g–i). For example, the high turbidity associated with
285 GMW1 spreads laterally beneath the pycnocline at R1 (Fig. 4 i). Turbidity does not consistently
286 map onto regions of local temperature minima; there are regions in the REMUS sections with
287 high turbidity but with temperatures above 0.9 °C (northeastern R1 below 80 m depth (Fig. 4 i)).
288 High turbidity in these regions may be due to other sources including suspended sediment
289 sourced from proglacial streams that enter SF as surface runoff near the northeastern end of R1
290 (Fig. 3) or iceberg discharge.

291 CTD casts 1–3 were taken closer to the SS face than the R5 transect during the same July
292 2012 field campaign (Fig. 3), and provide additional θ/S characteristics below the 100-m
293 REMUS depth limit (Fig. 6 a–c). These casts record deeper cold anomalies at the bottom of SF,
294 as well as cold excursions from ~40 to 80 m depth, similar to REMUS measurements (Fig. 6 a–
295 c). Overall the CTD profiles align well with REMUS measurements where coincident (above
296 100-m).

297 Further insight into the origins of GMW1 and GMW2 is found in θ/S space, where
298 GMW1 and GMW2 stand out as cold anomalies as compared to waters near the mouth of the
299 fjord (Figs. 5 d, 6 a, b). GMW1 and GMW2 are clustered at two distinct densities (Fig. 6 a, b).
300 At a density of $\sigma_\theta \approx 24.8 \text{ kg m}^{-3}$, where σ_θ is potential density less 1000 kg m^{-3} , GMW1 is lighter
301 than GMW2 ($\sigma_\theta \approx 25.5 \text{ kg m}^{-3}$) (Table 2, Fig. 6 a, b). In general, GMW is fresher and more turbid
302 compared to ambient waters, consistent with fjord waters mixing with submarine melt and
303 subglacial discharge. If we assume that both GMW1 and GMW2 are driven by subglacial
304 discharge plumes that emerged at the grounding line, then we can assume that the bulk of the
305 entrainment was of deeper waters at densities of $\sigma_\theta = 25.5\text{--}26.5 \text{ kg m}^{-3}$ (Fig. 6 a, b). In θ/S space,
306 GMW is further identified with the use of meltwater and runoff mixing lines (Figs. 5 c, d & 6 a–
307 c), which represent conservative mixing between ambient water and submarine melt or
308 subglacial discharge, respectively (Jenkins, 1999). Endpoints for the melt and runoff mixing
309 lines are set to properties observed by CTD cast 2 at grounding line depth (Figs. 3, 6 b). GMW1
310 and GMW2 are consistent with the transformation of ambient waters by mixing with submarine
311 melt and subglacial discharge, as they fall between the meltwater and runoff mixing lines in θ/S
312 space (Fig. 5 c, d & 6 a–c).

313 Thus, near the glacier we observe water masses not found in the outer fjord that we
314 attribute to glacier/ocean interactions (Jenkins et al., 2010; Straneo et al., 2011). We observe two
315 distinct GMW that are both colder, fresher, and more turbid compared to ambient waters at
316 similar depths (Figs. 5 a–c, 6 a, b) but are located in different regions of the fjord (Fig. 3).
317 GMW1, observed in the southwestern ends of R1–R5, is considerably fresher and lighter than the
318 colder GMW2 observed in the northeastern ends of R1–R5 (Figs. 3, 6 a, b, Table 2). The lighter
319 GMW1 ($\sigma_\theta \approx 24.8$) is observed at an equilibrium depth of 35–60 m, while the denser GMW2 (σ_θ
320 ≈ 25.5) has a deeper equilibrium depth of 50–70 m (Table 2), suggesting that GMW1 contains a
321 higher fraction of subglacial runoff than GMW2 (See section 4.3). We further elucidate GMW1
322 and GMW2 origins in the following section on the SS catchment and subglacial discharge across
323 the SS terminus.

324

325 **4.2. SS catchment and subglacial discharge across SS terminus**

326 The $400 \pm 50 \text{ km}^2$ area SS catchment extends 15-km up the basal valley beneath the 6-km
327 wide SS outlet glacier snout and widens under inland ice, reaching a maximum inland extent of
328 35-km just above the 900 m a.s.l. ice-sheet surface elevation contour (Fig. 7 a, Table 3). Bedrock
329 basins that steer subglacial water to the southwest delineate the southern boundary of the
330 catchment (Fig. 7 a). The northern extent of the catchment is bounded by the Alanngorliup
331 sermia outlet glacier catchment parallel to SS (Fig. 7 a). Three sub-catchments—C1, C2, and
332 C3—are delineated within the SS catchment from binning $-\nabla\Phi_h$ streamline endpoints along the
333 SS face in both the MBM2014 and BBM2013 analyses (Fig. 7 a). The main difference between
334 the MBM2014 and BBM2013 analyses is the size of the C1 subcatchment (BBM2013 33%

335 larger), with the BBM2013 analysis delineating the northern inland extent of C1 into a region the
336 MBM2014 analysis places in the Alanngorliup sermia catchment (Figs. 1 & 7 a, Table 3).

337 The three sub-catchments delineate three sections along the terminus (Fig. 7 a), with each
338 section mapping onto a directly observed or inferred subglacial meltwater discharge channel
339 (D1, D2, and D3 in Fig. 3). Subcatchment C1, the largest sub-catchment at 269 km² area
340 (MBM2014) discharges along the middle of the terminus at discharge location D1, while
341 subcatchment C2 and C3 discharge along the northeastern and southwestern extents of the
342 terminus at D2 and D3, respectively (Fig. 3). D1 and D2 align with two distinct bathymetric
343 troughs of 150 and 132-m depth, respectively (Table 3), bounded by bathymetry highs of 60 to
344 40 meters depth in SF (Fig. 3). D1 and D2 also coincide with depressed glacier margin heights
345 along the terminus, enhanced ice sheet velocities (Joughin et al., 2013), and high calving flux
346 relative to the rest of the terminus. D1 is a particularly frequent calving region in comparison to
347 the rest of the terminus, as observed during our two field campaigns. At times, a turbulent,
348 sediment-rich plume reaches the fjord surface at D1, as observed in satellite images and during
349 subsequent fieldwork in July 2013 (Mankoff et al., submitted). While exhibiting similarly
350 frequent calving, terminus height, and velocity characteristics as D1, surface plumes have not
351 been observed at D2. Subcatchment C3 discharges beneath the slow-moving, southwestern
352 margin of the terminus at D3 (Fig. 3), through a visible, broad channel mouth at the fjord
353 surface, entering into a shallow region of SF (Table 3, Fig. 3).

354 Variability in calculated subglacial discharge for each subcatchment is controlled
355 primarily by temperature variability, with daily runoff rates a summation of melt and
356 precipitation across the catchment (van den Broeke et al., 2009) (Fig. 7 b, Table 3). During our
357 2012 field expedition, catchment runoff rates were slightly below the monthly July average, with

358 no above average temperature days falling within the sampling period (Fig. 7 b). Disregarding
359 the possibility for periods of subglacial water storage during the en- and subglacial transport of
360 runoff to the SS terminus, daily discharge rates across the terminus during the field expedition
361 are $146 \text{ m}^3 \text{ s}^{-1}$ (MBM2014 estimate) (Table 3). An additional though likely minor amount of
362 surface meltwater runoff enters the fjord through proglacial streams, which discharge at land-
363 terminating margins abutting SS (Fig. 2). Daily runoff discharges for C1 and C2 scale primarily
364 with area differences and are 115.78 and $20.62 \text{ m}^3 \text{ s}^{-1}$, respectively (MBM2014) (Table 3). As
365 error estimates for the RACMO2.3 runoff rates are not available, we take the standard deviation
366 of July 2012 daily discharge rates as a measure of the potential variation observed during the
367 field expedition (Table 3).

368

369 **4.3. Buoyant plume model for the SS/SF system**

370 As described above, we have found evidence for three main subglacial catchments
371 discharging runoff into SF at three locations along the terminus. The two prominent discharge
372 locations, D1 and D2, coincide with GMW1 and GMW2 observations. The picture that emerges
373 is that different properties of GMW1 and GMW2 are attributable to differences in subglacial
374 discharge magnitude at that location. Here, we use a buoyant plume model to investigate the
375 extent to which the two plumes' predicted characteristics compare with the GMW1 and GMW2
376 observations. Buoyant plume theory states that the growth of a plume is dictated by the plume's
377 buoyancy forcing, which can be due to subglacial discharge at the grounding line and/or
378 submarine melting along the terminus (Morton et al., 1956; Turner, 1979). The buoyancy forcing
379 of the plume determines the plume's vertical velocity and entrainment of ambient fjord waters
380 (Morton et al., 1956; Turner, 1979). A class of simple, one-dimensional buoyant plume models

381 has been used to investigate plume dynamics and terminus melt rates near glaciers (Hellmer and
382 Olbers, 1989; Jenkins, 1991, 2011). Solutions to these models estimate plume temperature,
383 salinity, vertical velocity, width, and intrusion depth, the depth at which the plume becomes
384 neutrally buoyant and changes from flowing vertically up the terminus to flowing horizontally
385 away from the terminus. Here we investigate D1 and D2 plume scenarios using the Jenkins
386 (2011) buoyant plume model adapted to a half-conical plume driven by a point-source.

387 The plume model uses conservation of the fluxes of mass, momentum, heat, and salt, to
388 calculate plume characteristics that are uniform in time and across-flow direction (Jenkins,
389 2011). Key initial conditions that we prescribe include an ice temperature of $-10\text{ }^{\circ}\text{C}$ (Lüthi et al.,
390 2002); fjord ambient temperature and stratification (Table 4); a vertical glacier face; and a
391 modeled subglacial discharge across the terminus, Q_{sg} (Table 4). Entrainment of ambient fjord
392 waters into the buoyant plume is modeled as a product of plume velocity, the sine of the ice
393 terminus slope (vertical for SS), and a theoretically defined entrainment coefficient (E_0) of 0.08
394 following Sciascia et al. (2013).

395 The buoyant plume model is calculated for D1 and D2 scenarios and evaluated based on
396 end plume temperature, salinity, and intrusion depth (Table 4). Ambient water properties are
397 defined by two CTD measurements of full water column temperature and salinity from nearby
398 D1 and D2 (CTD1 and CTD2, respectively, in Fig. 3). Temperature, salinity, and intrusion depth
399 at the end of the plume are found to be largely insensitive to varying ambient fjord water
400 properties if the ambient waters show strong summer stratification. We use the RACMO2.3-
401 derived estimates of subglacial discharge across the terminus at D1 and D2 ($\text{m}^3\text{ s}^{-1}$) (using
402 MBM2014 of average daily runoff during the field expedition ($\text{m}^3\text{ s}^{-1}$)) (Table 3).

403 Given the observed ocean stratification and the modeled subglacial discharge, the plume
404 model confirms that GMW1 should be notably fresher and lighter than GMW2 (Fig. 5 c, Table
405 4). This supports the conclusion that GMW1 and GMW2 are the result of two distinct discharge
406 locations with different subglacial discharge magnitudes. For the D2 scenario, the plume model
407 predicts end plume properties and neutrally buoyant depths (~31 m) that are aligned with the
408 GMW2 observations at similar depths (Fig. 5c, d). For the D1 scenario, the plume model predicts
409 end plume properties that are lighter and fresher than the observed GMW1 (Fig. 5 c, Tables 2 &
410 4). The predicted D1 plume would reach above the 20-m-deep pycnocline at neutral buoyancy
411 depth of ~14 m, (Table 4). With a minimum amount of overshoot, we might expect the D1 plume
412 to reach the surface or depths close enough to the surface to be visible during field observations.
413 In reality, the plume at D1 was not observed to reach the surface, and GMW1 was only observed
414 beneath the pycnocline (Fig. 4). There are several possible reasons for this discrepancy. First, the
415 plume model may have an incorrect entrainment parameterization. Second, the estimated
416 subglacial discharge could be incorrect. In addition, after detaching from the terminus at the
417 plume's intrusion depth, GMW spreads an additional 150 m away from the SS face before being
418 observed at R5. Over this time, we would expect lateral mixing to further dilute the GMW
419 properties. The plume model does not describe lateral mixing, as the model ends when the plume
420 reaches intrusion depth.

421

422 **5. Discussion**

423

424 **5.1. Subglacial catchments, discharge, and GMW observations**

425 Our analysis of the ocean data and subglacial catchments both suggest that there are two
426 primary subglacial discharge locations along the ice/ocean interface. On the outlet glacier
427 catchment side of the interface, the primary subcatchments, C1 and C2 (Fig. 7a), route
428 substantial (>90%) of the total SS meltwater runoff (Table 3) into the fjord across the grounding
429 line at discharge locations D1 and D2, respectively (Fig. 3). On the ocean side of the interface,
430 GMW1 and GMW2 are located near D1 and D2, respectively, and show fresher, colder waters
431 with high turbidity as compared to ambient fjord waters (Fig. 5 a, b). The properties of these
432 waters, in particular, are consistent with glacial modification due to significant injection of
433 runoff at depth as is expected from a localized discharge of meltwater at D1 and D2. Finally,
434 between D1 and D2, there is a 2-km stretch of the terminus where GMW show cold excursions
435 with low to high turbidity along R4 and R5 (Fig. 6 c). The formation of this GMW is less clear,
436 though in this region between subglacial discharge locations, GMW properties are more
437 indicative of submarine melt and limited subglacial discharge and/or lateral mixing of GMW1
438 and GMW2.

439 Although we lack observations within the plumes themselves in 2012, the ocean
440 observations of GMW suggest that these waters are produced by ambient fjord waters interacting
441 with a limited number of discrete plumes along the terminus. Our observations of GMW beneath
442 the pycnocline at a distance of ~150 m from the terminus suggest that the two plumes reach
443 neutral buoyancy beneath the fjord surface. Visual observations during the 2012 field campaign
444 confirm that the plumes did not reach the fjord surface during this time. In contrast, during the
445 July 2013 field campaign at SF, a vigorous, turbulent plume was observed to break through at the
446 fjord surface at D1 (Mankoff et al., submitted).

447 Differences in subglacial discharge magnitude entering the fjord at D1 and D2 is both
448 observed and predicted to result in water mass differences between GMW1 and GMW2. Fed by
449 subglacial discharge from the largest subglacial subcatchment, GMW1 is fresher and lighter than
450 GMW2 (Table 3, Figs. 5 a–d, 6 a, b). D2 receives roughly 20% of the subglacial discharge
451 magnitude at D1 (Table 3). This smaller subglacial discharge results in a relatively saltier and
452 heavier GMW2 in comparison to GMW1 (Figs. 5 a–d, 6 a, b). While a greater volume of
453 subglacial discharge leads to a fresher water mass, the strength of the resultant buoyant plume
454 also plays a role in near-ice water mass transformation. Plume theory predicts that a plume fed
455 by a greater amount of subglacial discharge will have a stronger buoyancy forcing, leading to
456 both faster entrainment of ambient waters and an increase in the fraction of subglacial discharge
457 in the plume (Jenkins, 2011; Straneo and Cenedese, 2015). In this fjord, the entrainment of
458 ambient waters into a plume results in GMW with temperatures and salinities that are warmer
459 and saltier than the subglacial discharge entering the fjord ($\theta = 0\text{ }^{\circ}\text{C}$, $S = 0\text{ PSU}$). The volume
460 fraction of entrained water for both D1 and D2 plumes is above 0.9 (Table 4), indicating that for
461 this fjord the plume temperature and salinity at neutral buoyancy depth are largely a function of
462 the entrained ambient water mass. Thus, overall, the greater subglacial discharge at D1 drives a
463 more vigorous plume that mixes with both IIW and SW, which results in GMW that is closer in
464 θ and S to SW than IIW (Table 2, Fig. 6 a). In contrast, smaller subglacial discharge at D2 drives
465 a less vigorous plume that mixes at deeper depths with only IIW, resulting in GMW that retains
466 the cold signature of subglacial discharge and submarine melting (Table 2, Fig. 6b).

467 Consistent with the ocean data, the plume model predicts end plume conditions at D1 are
468 fresher and lighter than those at D2 as they contain a greater amount of subglacial discharge (Fig.
469 5 d, Table 4). However, the end plume conditions from the Jenkins (2011) model for D1

470 scenarios are lighter than the GMW1 we observe (Fig. 5 c, Table 4). In addition to errors in the
471 plume model and subglacial discharge estimates, lateral mixing within ~150 m of the terminus is
472 a consideration for comparing the plume model results and observed GMW. Large amounts of
473 mixing with ambient waters likely occur once the plume detaches from the terminus and GMW
474 is exported away from the ice/ocean interface. This lateral mixing has been observed in other
475 marine terminating outlet glacier systems in Greenland, where GMW from an inferred localized
476 subglacial discharge location was found uniformly across the fjord in profiles taken ~200 m from
477 the terminus (Chauché et al., 2014).

478

479 **5.2. Observing the heterogeneous near-ice environment**

480 The coupling of near-ice observations and subglacial discharge routing is necessary for
481 understanding ice-ocean interactions at marine terminating outlet glaciers. While multiple recent
482 studies have observed GMW in fjords (Chauché et al., 2014; Inall et al., 2014; Johnson et al.,
483 2011; Mortensen et al., 2011; Straneo et al., 2011; Sutherland et al., 2014) and others have
484 measured and modeled runoff based on surface catchment area (Mernild et al., 2015), no studies
485 have directly linked the two sides of this interface or considered the role of basal routing on
486 catchment area. For this study, we pair near-ice observations and subglacial discharge routing to
487 show for the first time that the observed GMW characteristics align with the subglacial discharge
488 magnitudes from outlet glacier subcatchments.

489 Our results highlight the necessity of subsurface observations within the near-ice zone for
490 accurately characterizing the heterogeneous processes at the ice/ocean interface. We observe
491 heterogeneous, subsurface GMW as high turbidity, cold excursions in across-fjord sections as far
492 as 1.5 km from the SS terminus (Fig. 4). Further away from the terminus, only the cold excursion

493 at the density of GMW1 remains in the far-field profiles (Fig. 5 d). Thus, while in the near-ice
494 zone there are multiple subglacial discharge locations across the SS grounding line and different
495 types of GMW observed, only a modified GMW1 is identifiable in far-field profiles. Noble gas
496 observations of GMW in neighboring Greenland fjords observe a dilution of GMW as you move
497 away from the terminus, suggesting that GMW is highly diluted outside of the near-ice zone
498 (Beaird et al., 2015). Thus, the fact that only a modified GMW1 is detectable in the far-field
499 profiles is likely due to the larger volume flux of discharge from D1 entering the fjord as
500 compared to discharge from D2 (Table 4). Sill depth may be an additional factor impeding the
501 export of GMW2; GMW2 is observed at or barely above the 70-m sill depth, while GMW1 is
502 observed at shallower depths (Figs. 1 & 3, Table 2). The implication is that far-field
503 measurements only provide a partial representation of processes along the ice/ocean interface.

504 Similar to the single cold excursion observed in the ambient SF waters, many studies
505 have observed evidence of subsurface GMW uniformly distributed across fjord width outside of
506 the near-ice zone (Johnson et al., 2011; Mortensen et al., 2011; Straneo et al., 2011; Chauché et
507 al., 2014; Inall et al., 2014; Sutherland et al., 2014). Observations at Store and Rink glaciers as
508 close as ~200 m to termini identify one to a couple of surface and subsurface plumes along each
509 glacier termini (Chauché et al., 2014). However, the GMW observed 200 m from the termini is
510 uniform across the fjord (Chauché et al., 2014). While our observations of subglacial discharge
511 locations in SF are consistent with the low number of subglacial discharge locations found at
512 Store and Rink glaciers (Chauché et al., 2014), we are able to further differentiate and map types
513 of GMW to outlet glacier subcatchments.

514 The subsurface nature of the plumes and resultant GMW we observed is consistent with
515 multiple studies that have also observed subsurface GMW (Chauché et al., 2014; Inall et al.,

516 2014; Johnson et al., 2011; Mortensen et al., 2011; Straneo et al., 2011; Sutherland et al., 2014).
517 Together these findings drive home the point that plumes and other processes at the ice/ocean
518 interface actively driving submarine melt can and often do operate without creating an
519 expression on the fjord surface. Surface expressions of plumes have been detected at many
520 Greenland tidewater glaciers and invoked as evidence for runoff release from the ice sheet into
521 fjords and proglacial streams (Chu et al., 2009; Tedstone and Arnold, 2012), and have even been
522 proposed as a potentially useful remote measure of runoff variability (Chu et al., 2012).
523 However, our observations of plumes and GMW that reach neutral buoyancy beneath the
524 pycnocline suggest in many cases this relationship does not hold true. The magnitude of
525 subglacial discharge entering a fjord, fjord stratification, and fjord depth have all been shown to
526 affect whether a plume reaches the surface (Sciascia et al., 2013). The absence of plume surface
527 expression does not negate the presence of subglacial discharge plumes that may be driving
528 significant submarine melt and circulation along a tidewater terminus. Thus, across-fjord
529 subsurface observations within the near-ice zone provide the most comprehensive
530 characterization of ice/ocean interactions in Greenland fjords.

531

532 **5.3. Observational constraints for modeling the heterogeneous near-ice environment**

533 While spatial distribution of subglacial discharge is a critical component for estimating
534 submarine melt rates at marine terminating outlet glaciers in numerical models (Slater et al.,
535 2015), we have few observations to constrain subglacial discharge scenarios. Model
536 configurations of subglacial discharge for major Greenland outlet glaciers range from a
537 distributed subglacial system where equal amounts of subglacial discharge emerge across the
538 entire grounding line width (Jenkins, 2011; Sciascia et al., 2013), to partitioning subglacial

539 discharge between a number of equally-spaced plumes along the terminus (Kimura et al., 2014;
540 Slater et al., 2015), to routing all subglacial discharge through a single subglacial channel
541 emerging in one, central plume (Slater et al., 2015; Xu et al., 2013). While all these models,
542 which share the same melt parameterization, agree that submarine melt rates increase with
543 increasing subglacial discharge (Jenkins, 2011; Kimura et al., 2014; Sciascia et al., 2013; Slater
544 et al., 2015; Xu et al., 2012, 2013), the amount and distribution of the increased melting depends
545 on the largely unknown pattern of subglacial discharge (Straneo and Cenedese, 2015). Most
546 recently, Slater et al. (2015) concluded that a distributed system yields as much as 5 times more
547 submarine melting than a channelized system consisting of a few plumes along the terminus.
548 Thus, spatial distribution of subglacial melt is critically important for accurately estimating
549 submarine melt rates in a numerical model (Slater et al., 2015; Straneo and Cenedese, 2015).

550 For this system, we observe at least two, localized areas of subglacial discharge separated
551 by wide areas of the terminus with little to no subglacial discharge. Our survey interval was
552 limited to peak summer conditions, when one would expect channelized subglacial discharge.
553 Observations during other times of the year, in particular prior to and during the onset of
554 meltwater runoff early in the melt season, as well as towards the end of the melt season when
555 runoff is reduced again, would be useful to more fully characterize the seasonally evolving
556 magnitude and type of subglacial discharge in this environment. A simple subglacial meltwater
557 routing model using MBM2014, the GIMP ice sheet surface digital elevation model, and
558 RACMO2.3 runoff estimates was able to predict the number, approximate location, and relative
559 magnitude and type of subglacial discharge locations. And while this subglacial catchment
560 delineation method should be supplemented with ocean measurements and field observations
561 where possible, in many cases it may prove a useful first order approximation of the spatial

562 distribution of subglacial discharge at other marine terminating outlet glaciers where fjord
563 observations are lacking or difficult to obtain.

564

565 **6. Conclusions**

566 Hydrographic surveys completed by an AUV in Sarqardleq Fjord provide several new
567 observational insights to the characteristics and distribution of near-ice GMW in a shallow-silled,
568 moderate-sized west Greenland fjord. Overcoming navigation difficulties in the acoustically
569 noisy, iceberg-filled fjord, the AUV covered a large portion of the near-ice waters along the
570 terminus. AUV observations provide the most comprehensive and spatiotemporally detailed
571 snapshots of across-fjord hydrography in the near-ice zone to date. From these measurements we
572 identified two types of GMW that map onto two plumes based on θ/S /turbidity near-ice
573 properties and subcatchment runoff estimates. The two plumes are, notably, not observed to
574 reach the surface in the fjords, but attain neutral buoyancy beneath the pycnocline of the strongly
575 stratified summer fjord conditions.

576 Our observations detail how mixing processes at the ice/ocean interface driven by either
577 submarine melting and/or plumes fed by subglacial discharge can produce GMW that is colder,
578 fresher, and at times more turbid than ambient fjord waters. An idealized plume model for
579 plumes fed by a range of RACMO2.3-derived subglacial discharges appropriate for the two
580 plumes observed in this fjord is qualitatively consistent with the largest subglacial discharge
581 being associated with the lighter, fresher glacially modified watermass. The characterization of
582 GMW and subglacial catchments for this outlet glacier system provides critical observational
583 constraints on the widely varying subglacial discharge scenarios employed by the current set of
584 submarine melt modeling studies. Results supply near-ice observations abutting one Greenland

585 Ice Sheet outlet glacier, though the continued investigation of other Greenland outlet glaciers is
586 much needed to ultimately move towards an accurate representation of oceanic forcing at outlet
587 glacier termini and an improved understanding of the ice sheet's outlet glacier dynamics.

588 **Acknowledgements**

589 Support was provided by the National Science Foundation's Office of Polar Programs (NSF-
590 OPP) through PLR-1418256 to F.S., S.B.D. and A.J.P., PLR-1023364 to S.B.D., and through the
591 Woods Hole Oceanographic Institution Ocean and Climate Change Institute Arctic Research
592 Initiative to F.S., S.B.D., and A.J.P. L.A.S. was also supported by a National Science Foundation
593 Graduate Research Fellowship. S.B.D was also supported by the Woods Hole Oceanographic
594 Institution James E. and Barbara V. Moltz Research Fellowship. M.M. was supported by the
595 National Aeronautics and Space Administration's (NASA) Cryospheric Sciences Program
596 through NNX15AD55G. The authors would like to acknowledge Michiel van den Broeke for
597 providing RACMO output; Jeff Pietro and John Kemp of the WHOI Mooring Operations,
598 Engineering and Field Support Group, and Rebecca H. Jackson and Ove Villadsen for their help
599 during the 2012 field operations; Clark Richards for guidance using the Barnes Objective
600 Analysis; Kenneth D. Mankoff for conversations on plumes in Sarqardleq Fjord; Nicholas L.
601 Beaird for conversations on glacially modified waters in Greenland fjords; and Adrian Jenkins
602 and Claudia Cenedese for providing the plume model code and discussing its application.

603

604 **Author contributions**

605 F.S., S.B.D., and A.J.P. conceived the study. F.S., S.B.D., and A.L.K. performed the fieldwork.
606 A.J.P., A.L.K., and L.A.S. processed the REMUS data. L.A.S., F.S., S.B.D., and A.J.P. analyzed
607 the REMUS and CTD data. L.A.S. created the bathymetry map. M.M. provided the reprocessed
608 bedrock elevation map. L.A.S., F.S., S.B.D., and A.J.P. interpreted the results. L.A.S. wrote the
609 paper. All authors commented on the paper.

610

611 **Competing financial interests**

612 The authors declare no competing financial interests.

613

614 **References**

- 615 Andrews, L. C., Catania, G. A., Hoffman, M. J., Gulley, J. D., Lüthi, M. P., Ryser, C., Hawley,
616 R. L. and Neumann, T. A.: Direct observations of evolving subglacial drainage beneath the
617 Greenland Ice Sheet, *Nature*, 514(7520), 80–83, doi:10.1038/nature13796, 2014.
- 618 Bamber, J., van den Broeke, M., Ettema, J., Lenaerts, J. and Rignot, E.: Recent large increases in
619 freshwater fluxes from Greenland into the North Atlantic, *Geophys. Res. Lett.*, 39(19), 1–4,
620 doi:10.1029/2012GL052552, 2012.
- 621 Bamber, J. L., Griggs, J. a., Hurkmans, R. T. W. L., Dowdeswell, J. a., Gogineni, S. P., Howat,
622 I., Mouginot, J., Paden, J., Palmer, S., Rignot, E. and Steinhage, D.: A new bed elevation dataset
623 for Greenland, *Cryosph.*, 7(2), 499–510, doi:10.5194/tc-7-499-2013, 2013.
- 624 Banwell, A. F., Willis, I. C. and Arnold, N. S.: Modeling subglacial water routing at Paakitsoq,
625 W Greenland, *J. Geophys. Res. Earth Surf.*, 118(3), 1282–1295, doi:10.1002/jgrf.20093, 2013.
- 626 Barnes, S. L.: Applications of the Barnes Objective Analysis Scheme. Part I: Effects of
627 Undersampling, Wave Position, and Station Randomness, *J. Atmos. Ocean. Technol.*, 11, 1433–
628 1448, 1994.
- 629 Beaird, N., Straneo, F. and Jenkins, W.: Spreading of Greenland meltwaters in the ocean
630 revealed by noble gases, *Geophys. Res. Lett.*, 42, doi:10.1002/2015GL065003, 2015.
- 631 Box, J. E., Yang, L., Bromwich, D. H. and Bai, L.-S.: Greenland Ice Sheet Surface Air
632 Temperature Variability: 1840–2007*, *J. Clim.*, 22(14), 4029–4049,
633 doi:10.1175/2009JCLI2816.1, 2009.
- 634 Van den Broeke, M., Bamber, J., Ettema, J., Rignot, E., Schrama, E., van de Berg, W. J., van
635 Meijgaard, E., Velicogna, I. and Wouters, B.: Partitioning recent Greenland mass loss., *Science*,
636 326(5955), 984–986, doi:10.1126/science.1178176, 2009.
- 637 Chandler, D. M., Wadham, J. L., Lis, G. P., Cowton, T., Sole, A., Bartholomew, I., Telling, J.,
638 Nienow, P., Bagshaw, E. B., Mair, D., Vinen, S. and Hubbard, A.: Evolution of the subglacial
639 drainage system beneath the Greenland Ice Sheet revealed by tracers, *Nat. Geosci.*, 6(4), 1–4,
640 2013.
- 641 Chauché, N., Hubbard, A., Gascard, J. C., Box, J. E., Bates, R., Koppes, M., Sole, A.,
642 Christoffersen, P. and Patton, H.: Ice–ocean interaction and calving front morphology at two
643 west Greenland tidewater outlet glaciers, *Cryosph.*, 8(4), 1457–1468, doi:10.5194/tc-8-1457-
644 2014, 2014.
- 645 Chu, V. W., Smith, L. C., Rennermalm, A. K., Forster, R. R. and Box, J. E.: Hydrologic controls
646 on coastal suspended sediment plumes around the Greenland ice sheet, *Cryosph. Discuss.*, 5,
647 2365–2407, doi:10.5194/tcd-5-2365-2011, 2012.

- 648 Chu, V. W., Smith, L. C., Rennermalm, A. K., Forster, R. R., Box, J. E. and Reehy, N.: Sediment
649 plume response to surface melting and supraglacial lake drainages on the Greenland ice sheet, *J.*
650 *Glaciol.*, 55, 1072–1082, doi:10.3189/002214309790794904, 2009.
- 651 Cuffey, K. M. and Patterson, W. S. B.: *The Physics of Glaciers*, 4th ed., Elsevier., 2010.
- 652 Enderlin, E., Howat, I. M. and Jeong, S.: An improved mass budget for the Greenland ice sheet,
653 *Geophys. Res. Lett.*, 41, 866–872, doi:10.1002/2013GL059010, 2014.
- 654 Fountain, A. G. and Walder, J. S.: Water flow through temperate glaciers, *Rev. Geophys.*,
655 36(97), 299, doi:10.1029/97RG03579, 1998.
- 656 Gladish, C., Holland, D. M., Rosing-Asvid, A., Behrens, J. W. and Boje, J.: Oceanic Boundary
657 Conditions for Jakobshavn Glacier. Part I: Variability and Renewal of Ilulissat Icefjord Waters,
658 2001–14, *J. Phys. Oceanogr.*, doi:10.1175/JPO-D-14-0044.1, 2015a.
- 659 Gladish, C. V., Holland, D. M. and Lee, C. M.: Oceanic Boundary Conditions for Jakobshavn
660 Glacier. Part II: Provenance and Sources of Variability of Disko Bay and Ilulissat Icefjord
661 Waters, 1990– 2011, *J. Phys. Oceanogr.*, 45(2003), 33–63, doi:10.1175/JPO-D-14-0045.1,
662 2015b.
- 663 Hellmer, H. H. and Olbers, D. J.: A two-dimensional model for the thermohaline circulation
664 under an ice shelf, *Antarct. Sci.*, 1(4), 325–336, doi:10.1017/S0954102089000490, 1989.
- 665 Hewitt, I. J., Schoof, C. and Werder, M. A.: Flotation and free surface flow in a model for
666 subglacial drainage. Part 2. Channel flow, *J. Fluid Mech.*, 702, 157–187.
- 667 Holland, D. M., Thomas, R. H., de Young, B., Ribergaard, M. H. and Lyberth, B.: Acceleration
668 of Jakobshavn Isbræ triggered by warm subsurface ocean waters, *Nat. Geosci.*, 1(10), 659–664,
669 doi:10.1038/ngeo316, 2008.
- 670 Howat, I. M., Negrete, A. and Smith, B. E.: The Greenland Ice Mapping Project (GIMP) land
671 classification and surface elevation data sets, *Cryosph.*, 8, 1509–1518, doi:10.5194/tc-8-1509-
672 2014, 2014.
- 673 Inall, M. E., Murray, T., Cottier, F. R., Scharrer, K. and Boyd, T. J.: Oceanic heat delivery via
674 Kangerdlugssuaq Fjord to the south-east Greenland ice sheet, *J. Geophys. Res. Ocean.*, 119,
675 631–645, doi:10.1002/2013JC009295, 2014.
- 676 Jackson, R. H., Straneo, F. and Sutherland, D. A.: Externally forced fluctuations in ocean
677 temperature at Greenland glaciers in non-summer months, *Nat. Geosci.*, 1–6,
678 doi:10.1038/ngeo2186, 2014.
- 679 Jenkins, A.: A one-dimensional model of ice shelf-ocean interaction, *J. Geophys. Res.*, 96(C11),
680 671–677, 1991.

- 681 Jenkins, A.: The Impact of Melting Ice on Ocean Waters, *J. Phys. Oceanogr.*, 29, 2370–2381,
682 1999.
- 683 Jenkins, A.: Convection-Driven Melting near the Grounding Lines of Ice Shelves and Tidewater
684 Glaciers, *J. Phys. Oceanogr.*, 41(12), 2279–2294, doi:10.1175/JPO-D-11-03.1, 2011.
- 685 Jenkins, A., Dutrieux, P., Jacobs, S. S., McPhail, S. D., Perrett, J. R., Webb, A. T. and White, D.:
686 Observations beneath Pine Island Glacier in West Antarctica and implications for its retreat, *Nat.*
687 *Geosci.*, 3(7), 468–472, doi:10.1038/ngeo890, 2010.
- 688 Johnson, H. L., Münchow, A., Falkner, K. K. and Melling, H.: Ocean circulation and properties
689 in Petermann Fjord, Greenland, *J. Geophys. Res. Ocean.*, 116, 1–18,
690 doi:10.1029/2010JC006519, 2011.
- 691 Joughin, I., Alley, R. B. and Holland, D. M.: Ice-Sheet Response to Oceanic Forcing, *Science*,
692 338, 1172–1176, 2012.
- 693 Joughin, I., Das, S. B., Flowers, G. E., Behn, M. D., Alley, R. B., King, M. A., Smith, B. E.,
694 Bamber, J. L., van den Broeke, M. R. and van Angelen, J. H.: Influence of ice-sheet geometry
695 and supraglacial lakes on seasonal ice-flow variability, *Cryosph.*, 7(4), 1185–1192, 2013.
- 696 Kimura, S., Holland, P. R., Jenkins, A. and Piggott, M.: The Effect of Meltwater Plumes on the
697 Melting of a Vertical Glacier Face, *J. Phys. Oceanogr.*, 140917134924005, doi:10.1175/JPO-D-
698 13-0219.1, 2014.
- 699 Lewis, S. M. and Smith, L. C.: Hydrologic drainage of the Greenland Ice Sheet, *Hydrol.*
700 *Process.*, 23, 2004–2011, doi:10.1002/hyp, 2009.
- 701 Lüthi, M., Funk, M., Gogineni, S. and Truffer, M.: Mechanisms of fast flow in Jakobshavns
702 Isbræ, Greenland, Part III. Measurements of ice deformation, temperature and cross-borehole
703 conductivity in boreholes to the bedrock, *J. Glaciol.*, 48(162), 369–385, 2002.
- 704 Mankoff, K. D., Straneo, F., Cenedese, C., Das, S. B., Richards, C. G., and Singh, H.: Structure
705 and dynamics of a subglacial plume in a Greenland fjord, submitted *J. Geophys. Res.*.
- 706 Mernild, S. H., Holland, D. M., Holland, D., Rosing-Asvid, A., Yde, J. C., Liston, G. E. and
707 Steffen, K.: Freshwater Flux and Spatiotemporal Simulated Runoff Variability into Ilulissat
708 Icefjord, West Greenland, Linked to Salinity and Temperature Observations near Tidewater
709 Glacier Margins Obtained Using Instrumented Ringed Seals, *J. Phys. Oceanogr.*, 45, 1426–1445,
710 doi:10.1175/JPO-D-14-0217.1, 2015.
- 711 Moon, T. and Joughin, I.: Changes in ice front position on Greenland’s outlet glaciers from 1992
712 to 2007, *J. Geophys. Res.*, 113(F2), F02022, doi:10.1029/2007JF000927, 2008.

- 713 Morlighem, M., Rignot, E., Mouginot, J., Seroussi, H. and Larour, E.: Deeply incised submarine
714 glacial valleys beneath the Greenland ice sheet, *Nat. Geosci.*, 7, 18–22, doi:10.1038/ngeo2167,
715 2014.
- 716 Mortensen, J., Lennert, K., Bendtsen, J. and Rysgaard, S.: Heat sources for glacial melt in a sub-
717 Arctic fjord (Godthåbsfjord) in contact with the Greenland Ice Sheet, *J. Geophys. Res.*, 116,
718 doi:10.1029/2010JC006528, 2011.
- 719 Morton, B. R., Taylor, G. and Turner, J. S.: Turbulent Gravitational Convection from Maintained
720 and Instantaneous Sources, *Proc. R. Soc. A Math. Phys. Eng. Sci.*, 234(1196), 1–23,
721 doi:10.1098/rspa.1956.0011, 1956.
- 722 Motyka, R. J., Dryer, W. P., Amundson, J., Truffer, M. and Fahnestock, M.: Rapid submarine
723 melting driven by subglacial discharge, *LeConte Glacier, Alaska, Geophys. Res. Lett.*, 40(19),
724 5153–5158, doi:10.1002/grl.51011, 2013.
- 725 Nye, J. F.: Water flow in glaciers: jökulhlaups, tunnels and veins, *J. Glaciol.*, 17, 181–207, 1976.
- 726 Palmer, S., Shepherd, A., Nienow, P. and Joughin, I.: Seasonal speedup of the Greenland Ice
727 Sheet linked to routing of surface water, *Earth Planet. Sci. Lett.*, 302, 423–428,
728 doi:10.1016/j.epsl.2010.12.037, 2011.
- 729 Plueddemann, A. J., Kukulya, A. L., Stokey, R. and Freitag, L.: Autonomous Underwater
730 Vehicle Operations Beneath Coastal Sea Ice, *IEEE/ASME Trans. Mechatronics*, 17(1), 54–64,
731 2012.
- 732 Post, A., O’Neel, S., Motyka, R. and Streveler, G.: A Complex Relationship Between Calving
733 Glaciers and Climate, *EOS Trans.*, 92(37), 305–312, 2011.
- 734 Rignot, E. and Kanagaratnam, P.: Changes in the velocity structure of the Greenland Ice Sheet,
735 *Science*, 311, 986–990, doi:10.1126/science.1121381, 2006.
- 736 Röthlisberger, H.: Water pressure in intra- and subglacial channels, *J. Glaciol.*, 11(62), 177–203,
737 1972.
- 738 Schoof, C.: Ice-sheet acceleration driven by melt supply variability, *Nature*, 468(7325), 803–806,
739 2010.
- 740 Schumann, K., Völker, D. and Weinrebe, W. R.: Acoustic mapping of the Ilulissat Ice Fjord
741 mouth, West Greenland, *Quat. Sci. Rev.*, 40, 78–88, doi:10.1016/j.quascirev.2012.02.016, 2012.
- 742 Sciascia, R., Straneo, F., Cenedese, C. and Heimbach, P.: Seasonal variability of submarine melt
743 rate and circulation in an East Greenland fjord, *J. Geophys. Res. Ocean.*, 118, 2492–2506,
744 doi:10.1002/jgrc.20142, 2013.

- 745 Shepherd, A., Ivins, E. R., A, G., Barletta, V. R., Bentley, M. J., Bettadpur, S., Briggs, K. H.,
746 Bromwich, D. H., Forsberg, R., Galin, N., Horwath, M., Jacobs, S., Joughin, I., King, M. A.,
747 Lenaerts, J. T. M., Li, J., Ligtenberg, S. R. M., Luckman, A., Luthcke, S. B., McMillan, M.,
748 Meister, R., Milne, G., Mouginot, J., Muir, A., Nicolas, J. P., Paden, J., Payne, A. J., Pritchard,
749 H., Rignot, E., Rott, H., Sorensen, L. S., Scambos, T. A., Scheuchl, B., Schrama, E. J. O., Smith,
750 B., Sundal, A. V, van Angelen, J. H., van de Berg, W. J., van den Broeke, M. R., Vaughan, D.
751 G., Velicogna, I., Wahr, J., Whitehouse, P. L., Wingham, D. J., Yi, D., Young, D. and Zwally, H.
752 J.: A Reconciled Estimate of Ice-Sheet Mass Balance, *Science*, 338(6111), 1183–1189, 2012.
- 753 Shreve, R. L.: Movement of water in glaciers, *J. Glaciol.*, 11(62), 205–214, 1972.
- 754 Slater, D. A., Nienow, P. W., Cowton, T. R., Goldberg, D. N. and Sole, A. J.: Effect of near-
755 terminus subglacial hydrology on tidewater, *Geophys. Res. Lett.*, 42, 1–8,
756 doi:10.1002/2014GL062494.1., 2015.
- 757 Straneo, F. and Cenedese, C.: The Dynamics of Greenland’s Glacial Fjords and Their Role in
758 Climate, *Ann. Rev. Mar. Sci.*, 7, 89–112, doi:10.1146/annurev-marine-010213-135133, 2015.
- 759 Straneo, F., Curry, R. G., Sutherland, D. a., Hamilton, G. S., Cenedese, C., Våge, K. and Stearns,
760 L. a.: Impact of fjord dynamics and glacial runoff on the circulation near Helheim Glacier, *Nat.*
761 *Geosci.*, 4, 322–327, doi:10.1038/ngeo1109, 2011.
- 762 Straneo, F., Hamilton, G. S., Sutherland, D. A., Stearns, L. A., Davidson, F., Hammill, M. O.,
763 Stenson, G. B. and Rosing-Asvid, A.: Rapid circulation of warm subtropical waters in a major
764 glacial fjord in East Greenland, *Nat. Geosci.*, 3, 182–186, doi:10.1038/ngeo764, 2010.
- 765 Straneo, F. and Heimbach, P.: North Atlantic warming and the retreat of Greenland’s outlet
766 glaciers., *Nature*, 504(7478), 36–43, doi:10.1038/nature12854, 2013.
- 767 Straneo, F., Heimbach, P., Sergienko, O., Hamilton, G., Catania, G., Griffies, S., Hallberg, R.,
768 Jenkins, A., Joughin, I., Motyka, R., Pfeffer, W. T., Price, S. F., Rignot, E., Scambos, T., Truffer,
769 M. and Vieli, A.: Challenges to Understanding the Dynamic Response of Greenland’s Marine
770 Terminating Glaciers to Oceanic and Atmospheric Forcing, *Bull. Am. Meteorol. Soc.*, 94(8),
771 1131–1144, doi:10.1175/BAMS-D-12-00100.1, 2013.
- 772 Sutherland, D. A., Straneo, F. and Pickart, R. S.: Characteristics and dynamics of two major
773 Greenland glacial fjords, *J. Geophys. Res. Ocean.*, 119, 3767–3791, doi:10.1002/jgrc.20224,
774 2014.
- 775 Tedstone, A. J. and Arnold, N. S.: Automated remote sensing of sediment plumes for
776 identification of runoff from the Greenland ice sheet, *J. Glaciol.*, 58(210), 699–712,
777 doi:10.3189/2012JoG11J204, 2012.
- 778 Thomas, R., Frederick, E., Krabill, W., Manizade, S. and Martin, C.: Recent changes on
779 greenland outlet glaciers, *J. Glaciol.*, 55(189), 147–162, doi:10.3189/002214309788608958,
780 2009.

- 781 Turner, J. S.: Buoyancy effects in fluids, Cambridge University Press., 1979.
- 782 Van den Broeke, M., Bamber, J., Ettema, J., Rignot, E., Schrama, E., van de Berg, W. J., van
783 Meijgaard, E., Velicogna, I. and Wouters, B.: Partitioning recent Greenland mass loss., *Science*,
784 326(5955), 984–986, doi:10.1126/science.1178176, 2009.
- 785 Werder, M. A., Hewitt, I. J., Schoof, C. G. and Flowers, G. E.: Modeling channelized and
786 distributed subglacial drainage in two dimensions, *J. Geophys. Res. Earth Surf.*, 118(4), 2140–
787 2158, doi:10.1002/jgrf.20146, 2013.
- 788 Xu, Y., Rignot, E., Fenty, I., Menemenlis, D. and Flexas, M. M.: Subaqueous melting of Store
789 Glacier, west Greenland from three-dimensional, high-resolution numerical modeling and ocean
790 observations, *Geophys. Res. Lett.*, 40(17), 4648–4653, doi:10.1002/grl.50825, 2013.
- 791 Xu, Y., Rignot, E., Menemenlis, D. and Koppes, M.: Numerical experiments on subaqueous
792 melting of Greenland tidewater glaciers in response to ocean warming and enhanced subglacial
793 discharge, *Ann. Glaciol.*, 53(60), 1–6, doi:10.3189/2012/AoG60A139, 2012.

794 **Table 1: REMUS Missions in Sarqardleq Fjord**

795

Mission	Date	Local Time at Mission Start	Duration (h:mm)	Transect Sampling Path (m-depth)	Distance Traveled (km)
R1	7/18	21:10	1:28	Yo-Yo = 5-90	9.00
R2	7/21	15:37	3:41	Yo-Yo = 5-50; Fixed Depth=50, 70; Altitude = 10 m off bottom	23.11
R3	7/22	14:58	6:25	Yo-Yo = 5-55; Fixed Depth= 60, 70; Altitude = 10 m above bottom	41.36
R4	7/23	14:37	5:05	Yo-Yo = 5-50; Fixed Depth = 60, 70; Altitude = 10 m above bottom	30.93
R5	7/24	18:12	5:26	Yo-Yo 5-60; Fixed Depth=40, 55, 70; Altitude = 10 m above bottom	34.91

796

797

798 **Table 2: Water mass properties in Sarqardleq Fjord**
 799

Water mass	Surface Water (SW)	Ilulissat Icefjord Waters (IIW)	Glacially Modified Water 1 (GMW1)	Glacially Modified Water 2 (GMW2)
Depth range (m)	0–20	20–SF bottom	35–60	50–70
S (PSU)	21–30.5	32.5–33.5	30.8–31.5	31.1–32.3
θ (°C)	1.5–10	0.8–1.5	0.75–0.85	0.59–0.75
σ_θ ($\rho_\theta - 1000 \text{ kg m}^{-3}$)	16.0–24.3	25.9–26.7	24.6–25.1	24.8–25.8
Turbidity (NTU)	Low (<4 NTU)	Low (<4 NTU)	High (>9 NTU)	High (>9 NTU)
Origin/Formation	Local formation	Disko and Baffin Bay	Local formation	Local formation

800
 801

802 **Table 3: Saqqarliup sermia subcatchments and runoff estimates**
 803

Subcatchment	C1	C2	C3	SS ($\sum C1-3$)
Discharge location	D1	D2	D3	--
Bathymetry along catchment terminus				
Average depth (m)	116.4	101.5	39.9	--
Maximum depth (m)	150.4	131.8	49.9	--
<i>Morlighem et al. (2014) (MBM2014)</i>				
Catchment area (km ²)	268.74	47.97	23.31	340.02
Catchment area compared to SS (%)	79%	14%	7%	--
Catchment average daily runoff July 2012 $\pm \sigma_{JULY}$ (Q _{sg}) (m ³ s ⁻¹)	115.78 \pm 42.59	20.62 \pm 7.33	9.97 \pm 3.47	146.37 \pm 53.26
Average daily July runoff compared to SS (%)	79%	14%	7%	--
Catchment average daily runoff during the field expedition (DOY 200, 203–206) $\pm \sigma_{JULY}$ (Q _{sg}) (m ³ s ⁻¹)	88.70 \pm 42.59	16.10 \pm 7.33	7.89 \pm 3.47	112.69 \pm 53.26
<i>Bamber et al. (2013) (BBM2013)</i>				
Catchment area (km ²)	402	42	9	453
Catchment area compared to SS (%)	89%	9%	2%	--
Catchment average daily runoff July 2012 $\pm \sigma_{JULY}$ (Q _{sg}) (m ³ s ⁻¹)	171.01 \pm 64.27	17.47 \pm 6.40	3.72 \pm 1.36	192.20 \pm 71.75
Average daily July runoff compared to SS (%)	89%	9%	2%	--
Catchment average daily runoff during the field expedition (DOY 200, 203–206) $\pm \sigma_{JULY}$ (Q _{sg}) (m ³ s ⁻¹)	122.83 \pm 64.27	14.08 \pm 6.40	3.05 \pm 1.36	139.96 \pm 71.75

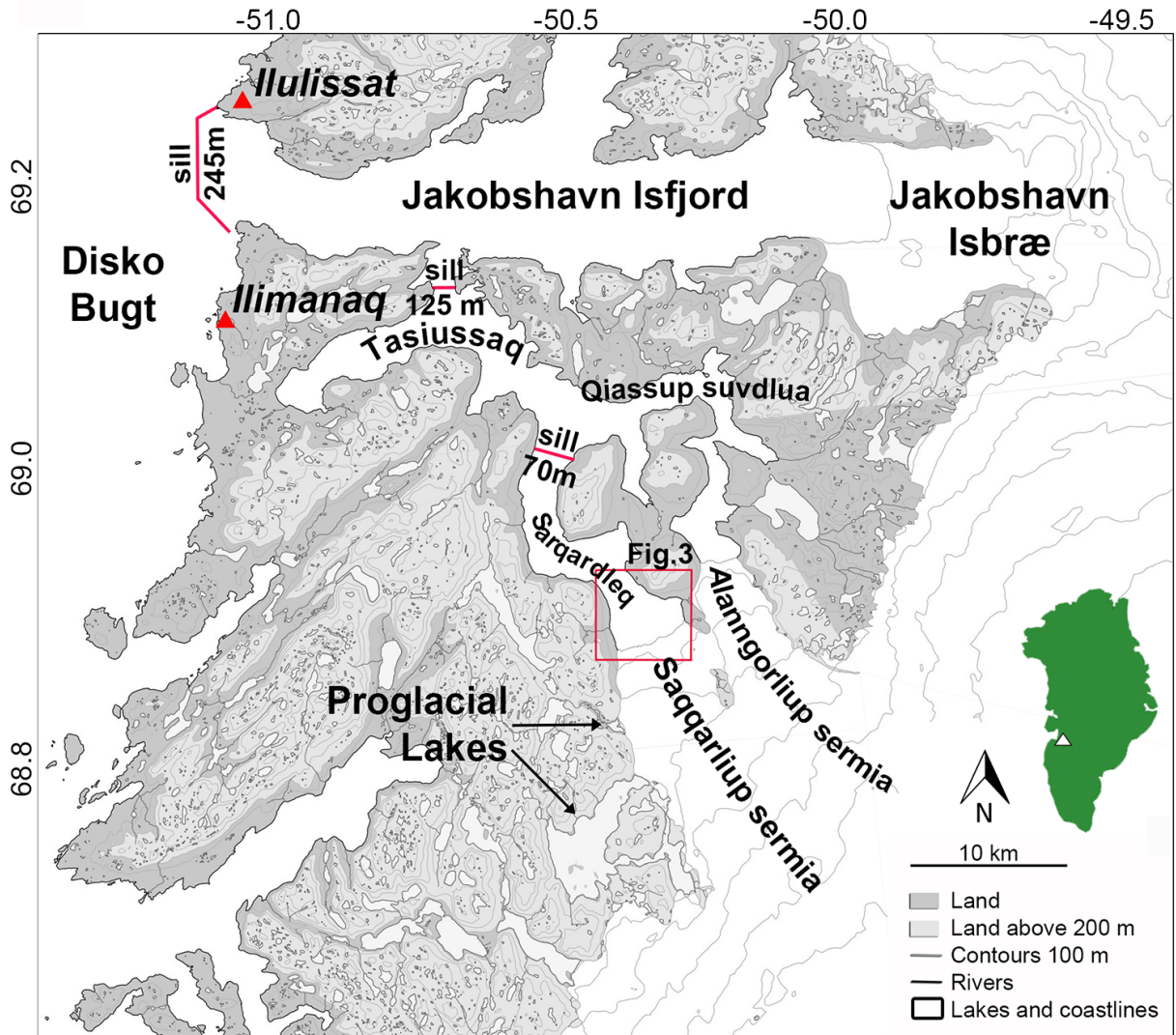
804
805

806 **Table 4. Buoyant plume model simulations for D1 and D2 scenarios at MBM2014**
 807 **subglacial discharge values. Plume θ and S ranges are plotted in Fig. 5 c, d.**
 808

	D1	D2
Ambient θ /S profile	CTD 1	CTD 2
Calving face depth (m)	153	140
Subglacial Discharge (Q_{sg}) ($\text{m}^3 \text{s}^{-1}$)	[46.11, 88.70, 131.29]	[8.77, 16.10, 23.43]
Plume θ ($^{\circ}\text{C}$) at neutral buoyancy depth	[0.82, 0.85, 0.84]	[0.83, 0.82, 0.82]
Plume S (PSU) at neutral buoyancy depth	[30.50, 29.72, 29.17]	[31.32, 30.88, 30.56]
Plume σ_{θ} ($\rho_{\theta} - 1000 \text{ kg m}^{-3}$) at neutral buoyancy depth	[24.34, 23.74, 23.30]	[24.90, 24.59, 24.35]
Neutral buoyancy depth (m)	[21.79, 14.03, 13.79]	[41.41, 31.23, 27.68]
Volume fraction of entrained water	[0.94, 0.94, 0.94]	[0.96, 0.96, 0.96]

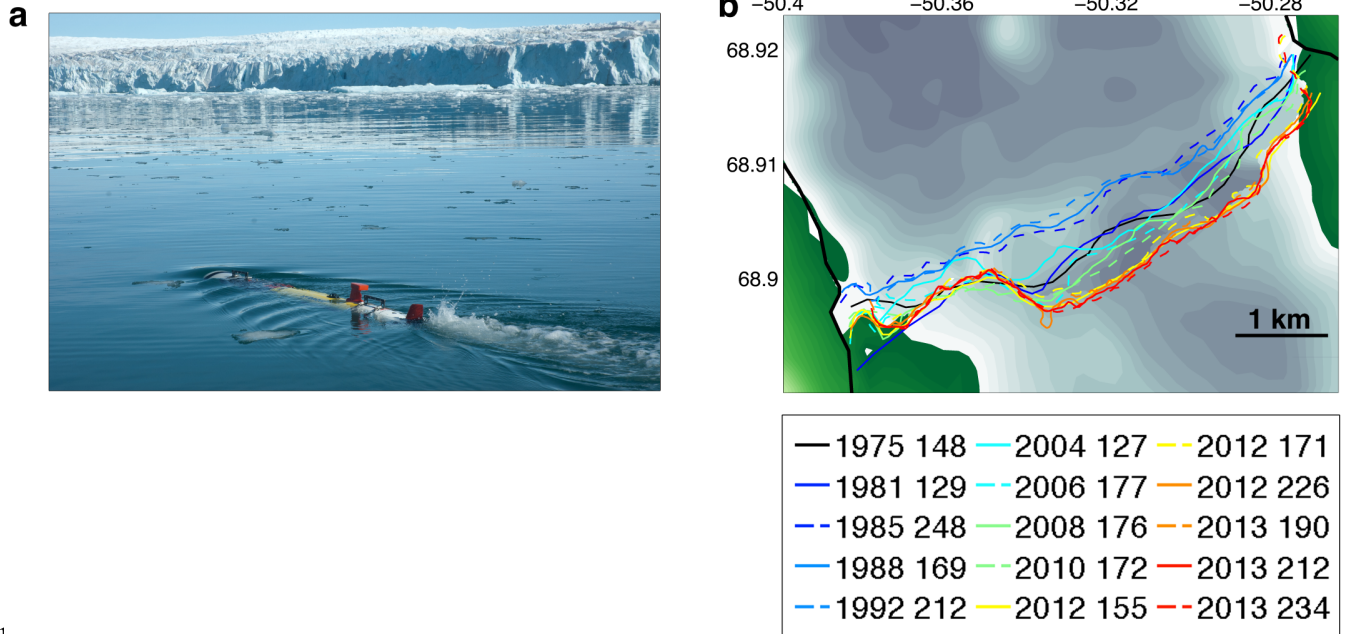
809

810

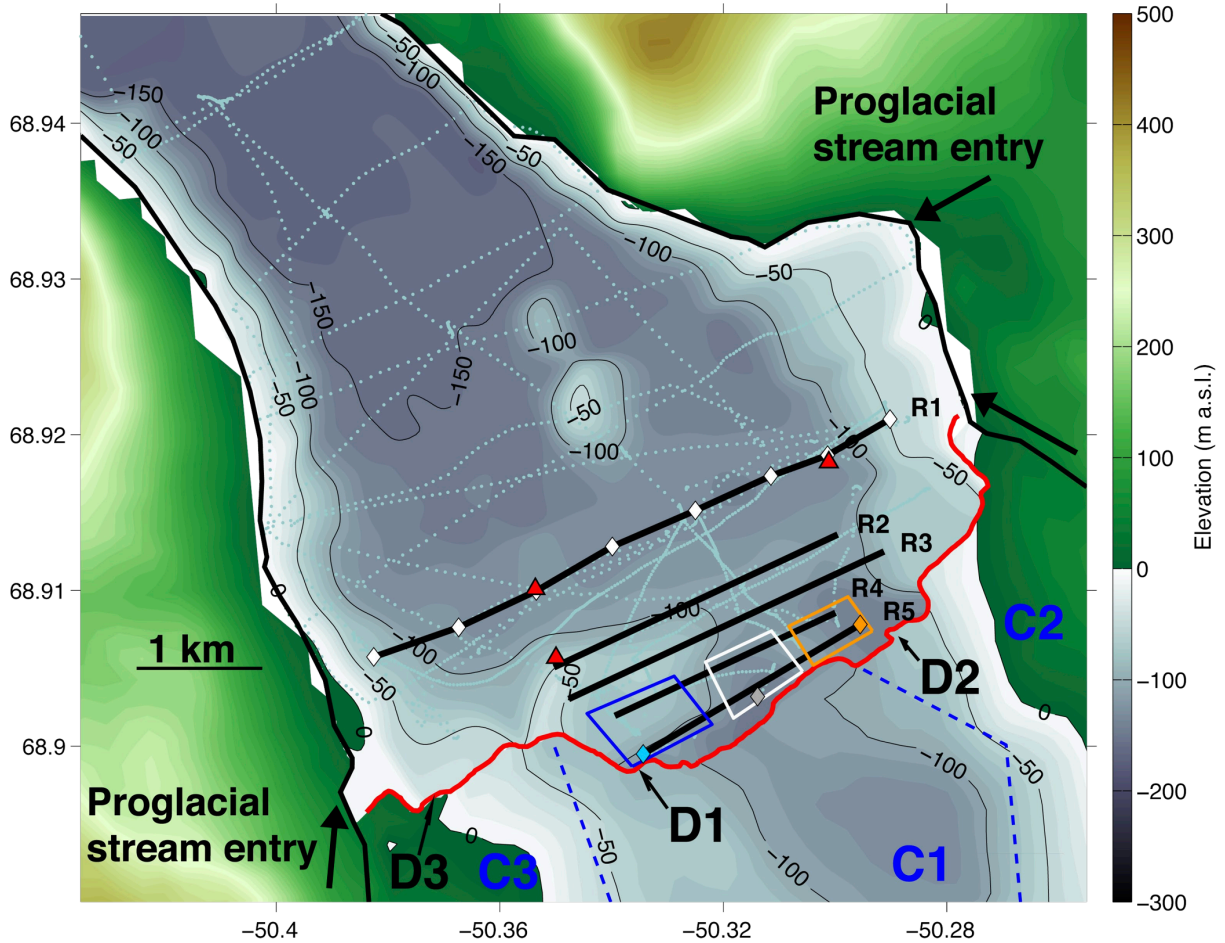


811

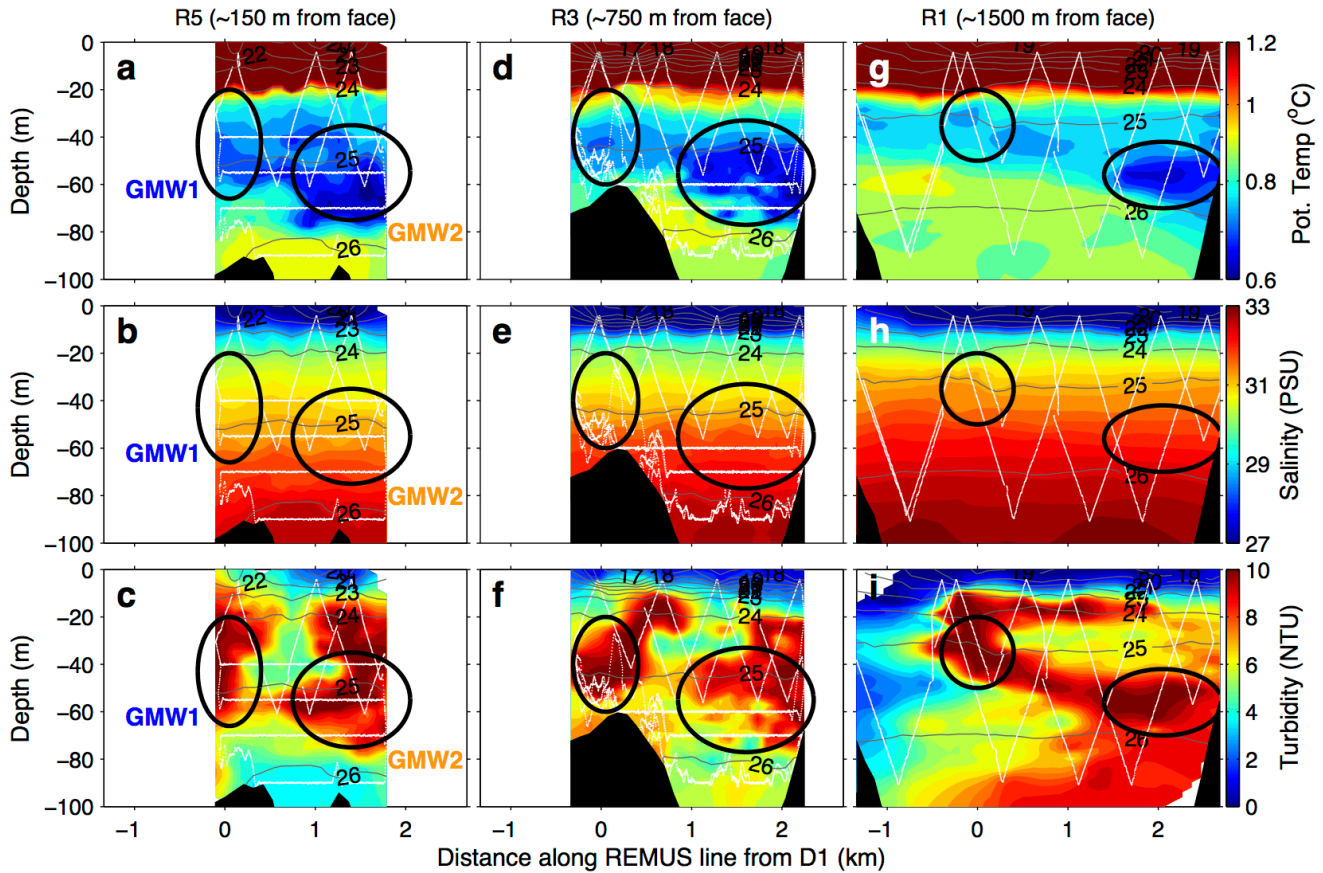
812 **Fig. 1. The Sarqardleq Fjord/Saqqarliup sermia outlet glacier system in West Greenland.** Modified
 813 from NunaGIS 1:100,000 map (Asiaq, Greenland Survey). Sill locations shown in red. Fig. 3 location
 814 shown in red box.



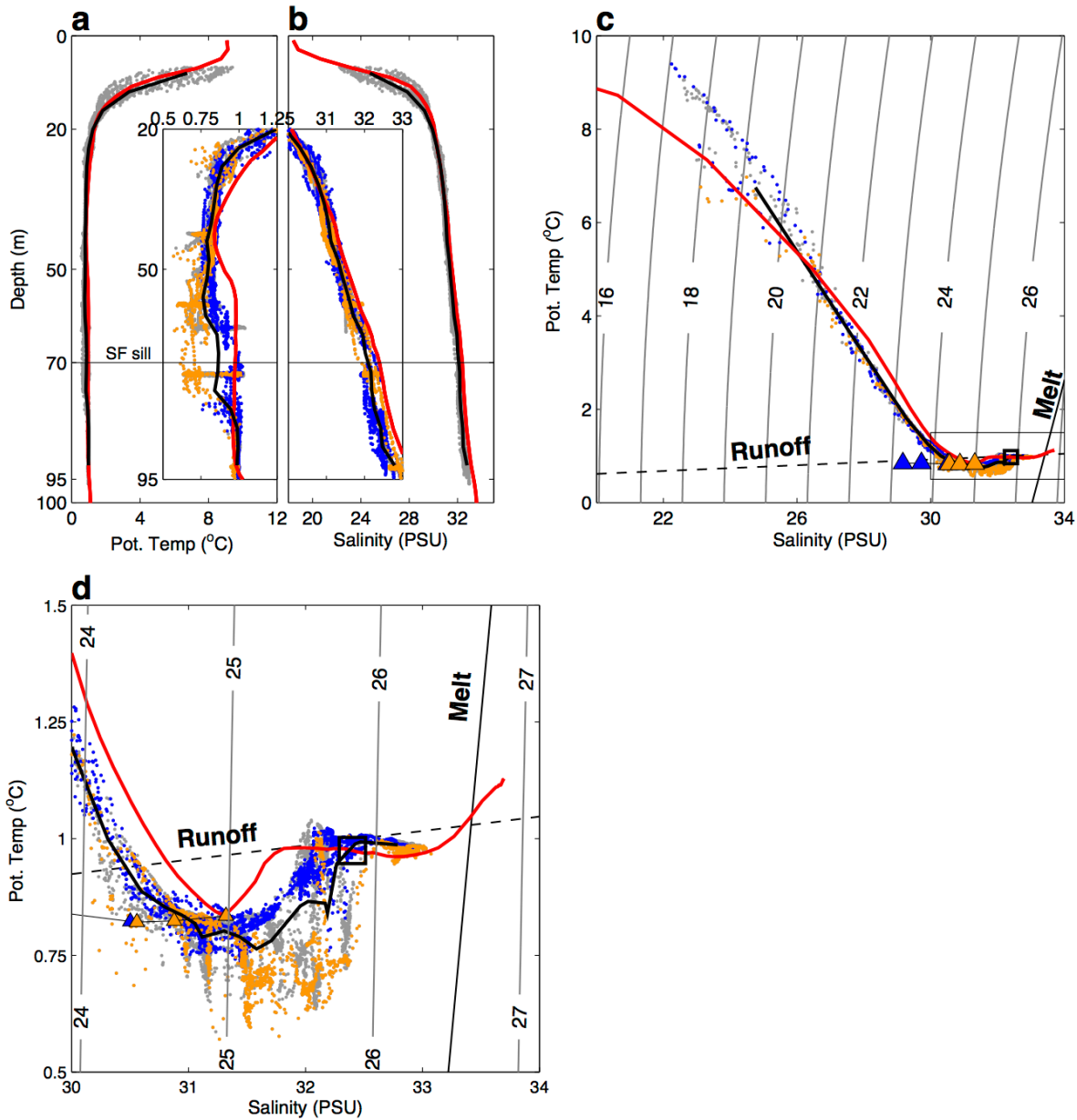
81
 816 **Fig. 2. REMUS-100 AUV and past Saqqarliup sermia terminus positions in Sarqardleq Fjord.** (a)
 817 REMUS-100 AUV before deployment in Sarqardleq Fjord. Note dense ice cover along Saqqarliup sermia
 818 terminus. (b) Saqqarliup sermia terminus 1975–2013 summertime positions digitized from the Landsat
 819 archive (<http://earthexplorer.usgs.gov/>) over fjord bathymetry and subglacial topography (see Fig. 3).
 820 Front position dates are listed in the legend as year and day of year.



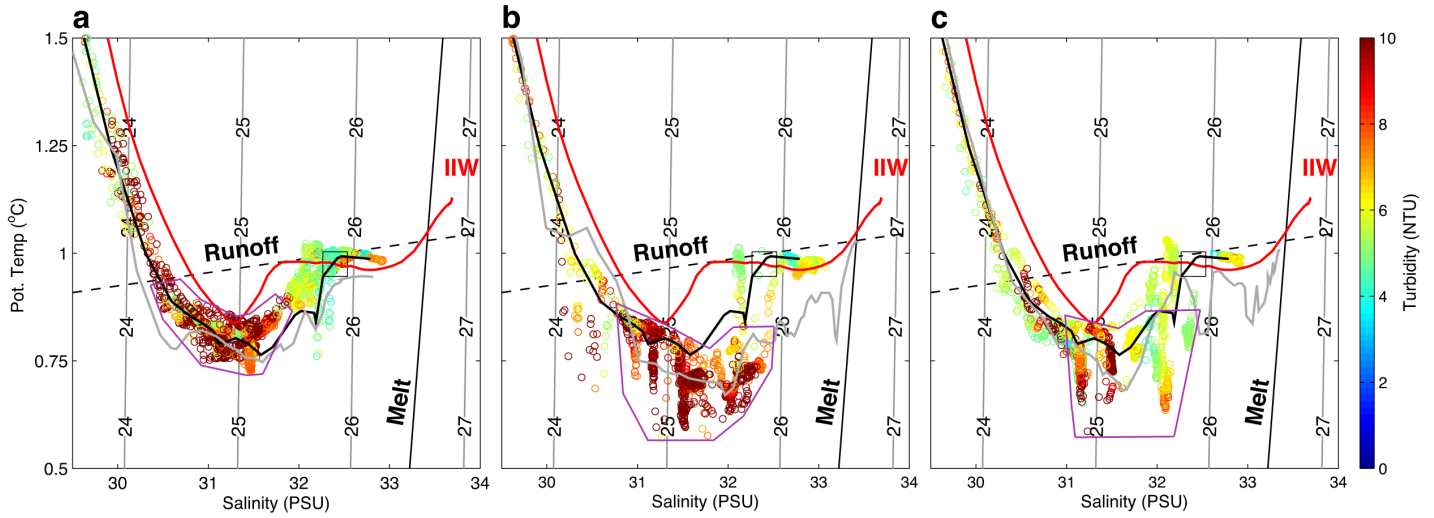
821
 822 **Fig 3. July 2012 Survey of Sarqardleq Fjord.** Sarqardleq Fjord bathymetry (10-meter colored contours
 823 below sea level within fjord) and Morlighem et al. (2014) bedrock elevation map (10-meter colored
 824 contours above and below sea level outside of fjord) are shown. The Saqqarliup sermia front position and
 825 coastline from a June 19, 2012 Landsat image are mapped in red and black lines, respectively. Depth
 826 measurements collected during July 2012 field operations used to create the Sarqardleq Fjord bathymetry
 827 are plotted as grey dots over the contoured bathymetry. REMUS transects R1–R5 are shown in black,
 828 with LBL transponders mapped with red triangles. Subglacial subcatchments C1, C2, and C3 dividing
 829 lines from MBM2014 analysis are mapped in dashed blue line, with the location of D1, D2, and D3
 830 subglacial discharge channels along the submerged terminus shown with thin black arrows. CTD casts are
 831 shown with diamonds: white diamonds are CTD casts along R1 used in REMUS cross-calibration, and
 832 the blue, gold, and grey diamonds are CTD casts 1, 2, and 3 that were taken along R5 within GMW1,
 833 GMW2, and the region between GMW1 and GMW2 (outlined in blue, gold, and white, respectively).
 834 Three proglacial stream entries to Sarqardleq Fjord are shown along the northeast and southwest fjord
 835 coastlines with thick black arrows.



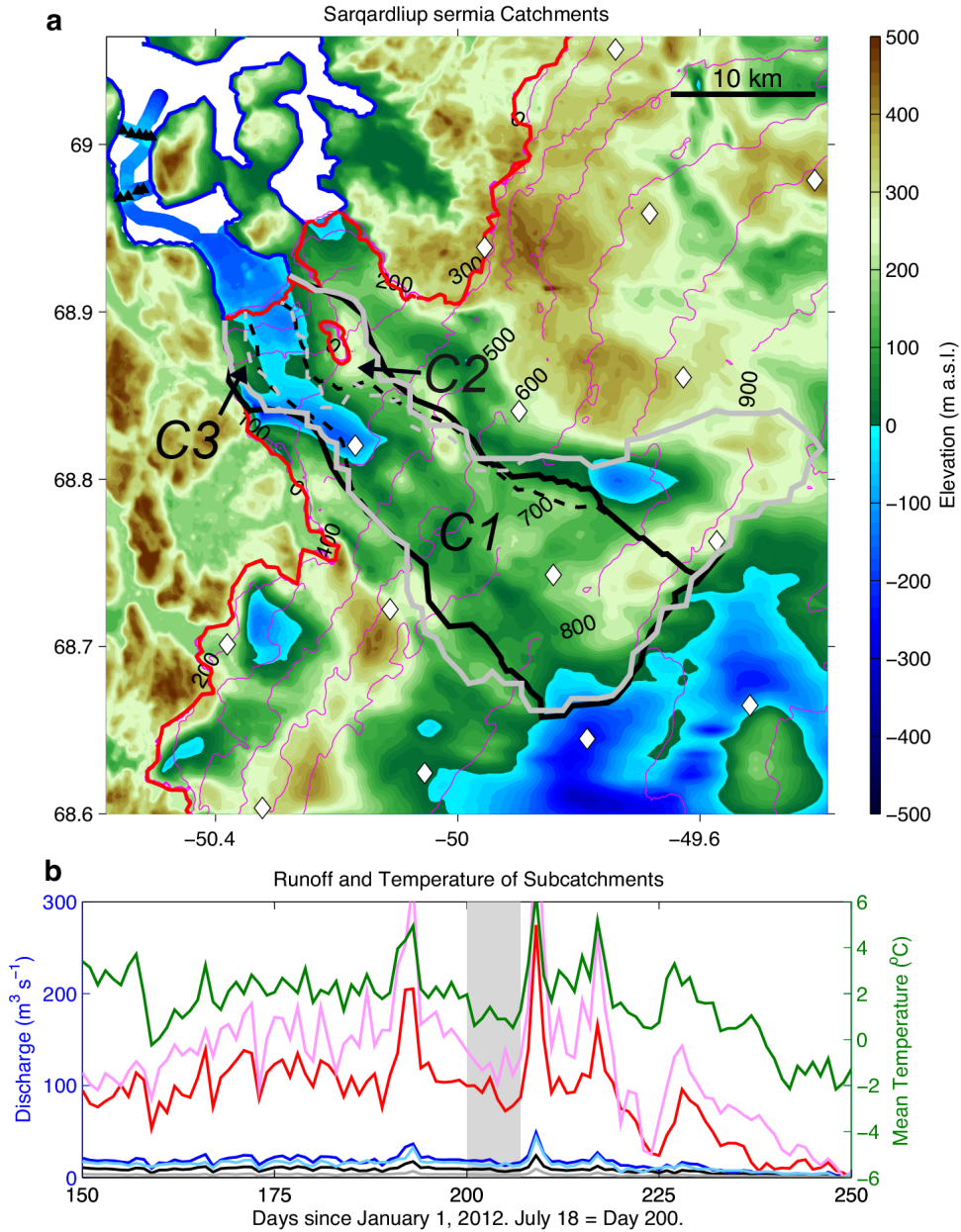
836
 837 **Fig. 4. Select REMUS Across-Fjord Sections.** θ ($^{\circ}\text{C}$), S (PSU), and turbidity (NTU) sections along
 838 REMUS lines (a–c) R5, (d–f) R3, and (g–i) R1 from 0 to 100 m depth. Sections are oriented looking
 839 away from the terminus, with the southwestern end of the section on the left. Across-fjord transect
 840 distance is plotted as horizontal distance along section, with 0 km located at the intersection of the
 841 REMUS section with an along-fjord line running from D1 to the southwestern LBL transponder along R1
 842 (Fig. 3). GMW1 and GMW2 regions identified by black ellipses, and labeled in blue and gold,
 843 respectively in a–c. Isopycnals plotted in grey, REMUS mission tracks shown in white (Table 1), and
 844 bathymetry shown in black (Fig. 3).



845
 846 **Fig 5. Glacially Modified Water in Sarqardleq Fjord.** θ ($^{\circ}\text{C}$) (a) and S (b) profiles for R4 and R5
 847 measurements over the full water-column depth (grey), with the average of R4 and R5 measurements and
 848 the ambient fjord waters in black and red, respectively. Panel a and b insets show same data from 20–95-
 849 m depth over a finer θ or S range, with measurements taken within the GMW1 and GMW2 regions along
 850 R4 and R5 (Fig. 3) shown in blue and gold, respectively. θ /S plots of R4 and R5 measurements (c) (colors
 851 same as in a and b), with melt and runoff mixing lines. Intersection for melt and runoff mixing lines set to
 852 CTD2 properties at grounding line depth (Fig. 6 b). Black square along ambient fjord water profile shows
 853 θ /S properties at sill depth (70 m). θ /S results for the Jenkins (2011) plume modeling (Table 4) of D1
 854 (blue triangles) and D2 (gold triangles) shown. (d) Same data as in c over finer θ /S range indicated by
 855 thin black box in c.
 856



858 **Fig. 6. Turbidity of Glacially Modified Waters.** θ ($^{\circ}\text{C}$) and S (PSU) profiles from the regions along R4
 859 and R5 outlined in blue (GMW1 region) (a), gold (GMW2 region) (b), and white (the region between
 860 GMW1 and GMW2) (c) in Figure 3, with turbidity plotted as the color of the point. CTD1 (a), CTD2 (b),
 861 and CTD3 (c) are plotted in grey. The GMW region in θ /S space is outlined in purple. The average of all
 862 R4 and R5 measurements and the ambient fjord waters are plotted in black and red, respectively. Black
 863 square along ambient fjord water profile shows θ /S properties at sill depth (70-m).



864
 865 **Fig. 7. Saqqarliup sermia catchments and discharge.** **a)** Estimated Saqqarliup sermia catchment (thick
 866 black line) and sub-catchments C1, C2, and C3 (dashed black line) from the MBM2014 analysis over
 867 Morlighem et al. (2014) bedrock elevation map (filled contours) and ice sheet surface (magenta contours).
 868 MBM2013 catchment and subcatchment outlines in thick solid and dashed grey lines, respectively. Ice
 869 sheet margin and coastlines shown in red and blue, respectively. RACMO2.3 11-km resolution grid points
 870 shown with white diamonds. Saqqardleq fjord bathymetry and outer Saqqardleq fjord CTD positions
 871 (black triangles) and depth measurements also shown. **b)** Daily C1, C2, and C3 subcatchment MBM2014
 872 RACMO2.3 discharge estimates (red, blue, and black lines, respectively) and daily average RACMO2.3
 873 temperature (green line) across the Saqqarliup sermia subcatchment C1 for DOY 150–250, 2012. Daily
 874 C1, C2, and C3 subcatchment MBM2013 RACMO2.3 discharge estimates in pink, cyan, and grey lines,
 875 respectively. Dates of REMUS and CTD sampling from DOY 200–207 marked by grey bar.